8

Research Article

Zhihui Xing*, Na Wang, Lei Fan, Li Shang, and Lianzhou Yu

Investigation of the corrosion performance of HVOF-sprayed WC-CoCr coatings applied on offshore hydraulic equipment

https://doi.org/10.1515/rams-2024-0066 received March 18, 2024; accepted October 17, 2024

Abstract: This study investigates the corrosion and erosion-corrosion performance of HVOF-sprayed WC-10Co-4Cr coatings for offshore hydraulic applications. By tuning kerosene (18.1–25.3 l·h⁻¹) and oxygen (820–990 l·min⁻¹) flow rates, coatings with optimal hardness (1200 HV0.3), porosity (0.35%), carbide retention (90%), and polarization resistance (15.2 kΩ·cm⁻²) are attained. In-flight diagnostics reveal that particle temperatures and velocities peak at 1,842°C and 799 m·s⁻¹, respectively, at stoichiometric combustion. Higher temperatures degrade electrochemical stability due to enriched binders when 30% of carbides decompose. The localized attack is mitigated as splatting from high-velocity particles eliminates 25% more porosity. With exposure to sulfate-reducing bacteria for 15 days, polarization resistance reduces to 12.4 kΩ·cm⁻² owing to biofilm formation, indicating self-healing effects from protective corrosion films. The optimized WC-CoCr coatings reduce corrosion rates under combined erosion and bacterial conditions by 86% compared to untreated steel substrates. This research provides a framework to customize HVOF coatings for demanding offshore conditions.

Keywords: HVOF parameters, carbide dissolution, electrochemical impedance, splat adhesion, self-healing oxide

1 Introduction

Hard chromium plating has been widely used to provide wear and corrosion protection for components in hydraulic

* Corresponding author: Zhihui Xing, School of Mechanical Engineering, Shenyang Urban Construction University, Shenyang, 110167, China, e-mail: xingzhihui20230817@163.com

Na Wang, Lei Fan, Li Shang, Lianzhou Yu: School of Mechanical Engineering, Shenyang Urban Construction University, Shenyang, 110167, China

systems used in offshore oil and gas operations [1]. However, the hexavalent chromium used in the plating process poses environmental and health hazards [2]. There has been increasing motivation to identify chrome-replacement coatings that can withstand the demanding offshore conditions without the toxic effects of chromium [3]. High-velocity oxyfuel (HVOF) thermal spraying is considered one of the most promising alternatives for producing protective coatings on offshore hydraulic machinery [4]. Compared to other thermal spray methods, HVOF produces very dense and well-adhered metallic, ceramic, and cermet coatings due to the high kinetic energy imparted by the hypersonic spray jet.

WC-CoCr coatings have shown excellent combined wear and corrosion resistance and are emerging as a leading candidate to replace hard chrome coatings in multiple applications [5–7]. The wear resistance stems from the hard tungsten carbide (WC) phase embedded in a tougher cobalt-chrome (CoCr) binder, while the alloyed CoCr matrix provides corrosion protection [8]. In recent years, several studies have investigated the corrosion properties of tungsten carbide coatings. Lekatou et al. [9] compared the corrosion and wear behavior of nanostructured and conventional WC-10Co-4Cr coatings deposited by HVOF on Al7075-T6 substrates. Kumar et al. [10] analyzed the effect of graphene nanoplatelets on the performance of WC-10Co-4Cr coatings applied to HSLA DH-36 steel using HVOF. Zhao et al. [11] investigated the influence of post-heat treatment on the wear and corrosion behavior of HVOF-sprayed WC-10Co-4Cr coatings. Kumar and Upadhyaya [12] evaluated the corrosion and wear performance of HVOLF-sprayed WC-10CO-4Cr coatings on geothermal turbine blades. Cao et al. [13] studied the low-temperature corrosion behavior of plasma transferred arc deposited WC-Co coatings on EH40 steel. While these studies provide valuable insights, there remains a need for systematic investigation focused on the combined effects of erosion, corrosion, and microbial activity, specifically in offshore environments. The corrosion behavior depends strongly on the coating microstructure, such as the carbide distribution, porosity levels, dissolution

of W and C in the binder, and the presence of detrimental phases [14]. Optimizing the HVOF process parameters tailors the thermal and kinetic histories of the in-flight particles, enabling control of the coating properties. Prolonged exposure to saline environments leads to general dissolution attack, while wear processes during hydraulic component operation expose fresh reactive surfaces. Offshore platforms and pipelines also face threats from biological influences such as sulfate-reducing bacteria [15,16]. It is therefore critical to systematically analyze the corrosion mechanisms affecting HVOF coatings across a range of anticipated offshore conditions.

This article aims to elucidate the slurry-erosion-corrosion and microbial corrosion performance of HVOF-sprayed WC-10Co-4Cr coatings in marine environments containing sand particles and sulfate-reducing bacteria. The specific influence of HVOF parameters including kerosene and oxygen flow rates on the in-flight particle characteristics and resulting coating properties are quantified. Detailed microstructural examination combined with electrochemical testing techniques provides insights into coating degradation mechanisms when subjected to erosion-corrosion in saline solutions and immersion in seawater inoculated with SRB cultures. The corrosion behavior metrics are benchmarked against stainless steel to quantify the performance advantages offered by optimized HVOF coatings. The comprehensive study will facilitate science-based design strategies for chrome-free protective coatings tailored to resist complex offshore operation conditions. Enhancing component durability and service life translates to significant cost reductions over the lifecycle of offshore hydraulic systems. Eliminating toxic hexavalent chrome also minimizes ecological impact to benefit marine life in offshore waters.

2 Materials and methods

2.1 Coating deposition

The protective coating studied in this work was a conventional WC-10wt%Co-4wt%Cr agglomerated and sintered cermet powder provided by Ding Hong Material Technology Co., LTD. The powder particles had a spherical morphology with sizes ranging from 10 to 38 μm . The powder feedstock was deposited onto rectangular substrates of AISI 4340 low alloy steel using a Praxair JP-8000 HVOF thermal spray system. The 100 mm \times 50 mm \times 6 mm steel substrates were grit-blasted with Al $_2$ O $_3$ particles to attain a 4–6 μm surface roughness profile prior to coating deposition. The steel substrates were selected based

on the recommendations provided in ASTM C633 – Standard Test Method for Adhesion or Cohesion Strength of Thermal Spray Coatings. These dimensions ensure sufficient surface area for coating adhesion while maintaining compatibility with the sample holders used in our corrosion testing setup. For each combination of HVOF spray parameters, a set of five identical samples were deposited to ensure repeatability and to provide specimens for the various characterization techniques employed in this study.

A kerosene-oxygen combustion flame was utilized for the HVOF process with kerosene flow rates ranging from 18.1 to 25.3 l·h⁻¹ and oxygen flow rates from 820 to 990 l·min⁻¹. The powders were injected into the combustor at a feed rate of 5 rpm using argon as the carrier gas. A robotic arm controlling the spray gun executed a raster pattern transverse to the 100 mm dimension of the substrates during coating deposition. The spray gun was maintained perpendicular to the substrates at a standoff distance of 300 mm. The number of passes and traverse speeds were adjusted to achieve a final coating thickness of 400 \pm 20 μ m. The in-flight particle diagnostics during spraying were captured using an Accurasprayg3 sensor fixed at 200 mm from the spray plume centerline. Cross-correlation of dual photodetector signals assessed particle velocities, while two-color optical pyrometry measured the average particle temperatures.

2.2 Coating characterization

The phase composition of the as-received feedstock powder and the deposited HVOF coatings were analyzed using X-ray diffraction (XRD) with a Siemens D500 instrument and Cu-K α radiation. Scanning electron microscopy (SEM) in backscattered electron imaging mode enabled the examination of powder morphology and detailed microstructural features of the coating cross-sections. The specimens were metallographically prepared and polished to a 0.02 μ m surface finish before microscopy. Image analysis of optical micrographs was utilized to quantify the porosity levels in the coatings by setting an appropriate threshold to differentiate between pores and coating material. Microhardness testing using a 300 gf Vickers indenter evaluated the mechanical properties of the as-sprayed coatings.

2.3 Corrosion testing

The electrochemical characteristics of the WC-CoCr coatings were measured using a Princeton Applied Research

VMP3 Potentiostat/Galvanostat controlled by a computer interface. A typical three-electrode setup was employed, with the coating sample serving as the 1 cm2 working electrode while a platinum mesh acted as the counter electrode. A saturated calomel electrode provided the reference potential. 0.1 N hydrochloric acid (HCl) was selected as an aggressive test solution to accelerate the corrosion reactions. Potentiodynamic polarization tests were conducted by sweeping the applied potential on the samples at a scan rate of 1 mV·s⁻¹ after allowing adequate time for open circuit stabilization. Corrosion current density (i_{corr}) and potential (E_{corr}) values were extracted from the measured polarization curves by Tafel analysis. Electrochemical impedance spectroscopy (EIS) analyzed the coating response under open circuit conditions across frequencies from 100 kHz to 10 mHz at 10 mV AC amplitude. Subsequent modeling via equivalent circuits provided insights into the corrosion mechanisms.

Immersion testing assessed the biocorrosion behavior in the presence of sulfate-reducing bacteria (SRB), which are commonly observed in offshore marine sediments. SRB cultures were enriched from marine mud samples in modified Postgate's medium C containing sodium lactate as the electron donor. The pH was adjusted to 7 prior to autoclaving the medium. Sterile agar plating generated an isolated SRB strain that was inoculated into sterile seawater obtained offshore from the test region. Coupon samples of the WC-CoCr coatings and stainless steel control samples were immersed in the SRB-containing actual seawater at 30°C for different durations of up to 15 days. The extent of bacterial colonization and biofilm formation on the sample surfaces was monitored using SEM.

3 Results and discussion

The effect of HVOF parameters on in-flight particle velocity/temperature is shown in Figure 1. The in-flight particle state during HVOF spraying plays a crucial role in determining the properties of the deposited coating. Key particle characteristics are the impact velocity and temperature, which were measured using the Accuraspray sensor for the range of kerosene and oxygen flow rates explored. As shown in Figure 1a, both particle velocity and temperature exhibit an increasing trend with a higher oxygen flow rate when maintaining the kerosene flow constant at 23.1 l·h⁻¹. The particle temperature reaches a maximum value of 1,842°C at an oxygen flow of 850 l·min⁻¹, corresponding to a stoichiometric combustion ratio (SCR) of 1.08. This indicates optimal combustion conditions, while excessive oxygen at higher flows has a cooling effect, thereby decreasing the flame and particle temperature. In contrast, continually increasing oxygen flow boosts the total gas volume passing through the torch nozzle [17]. This elevates the gas velocity, explaining the rise in particle velocities up to 793 m·s⁻¹ for the maximum tested oxygen flow rate of 990 l·min⁻¹.

The influence of kerosene flow rate at a constant oxygen rate reveals similar trends, as presented in Figure 1b. The particle temperature peaks at an intermediate kerosene value of $23.1\,l\cdot h^{-1}$, equivalent to the optimal SCR of 1.14. Lower quantities of kerosene result in incomplete combustion and insufficient thermal input to the particles [18]. Higher flows provide excess fuel that must vaporize to participate in combustion, thereby absorbing heat and reducing flame temperatures [19]. The velocity profile

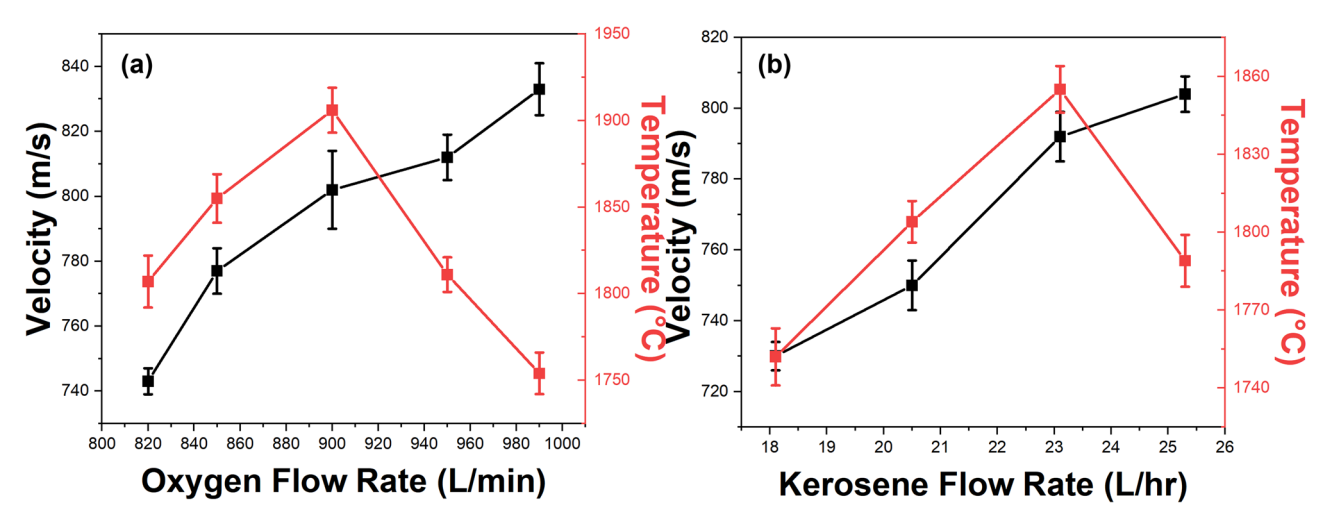


Figure 1: In-flight particle velocity and temperature during HVOF spraying at (a) fixed kerosene flow with varying oxygen flow and (b) fixed oxygen flow with varying kerosene flow.

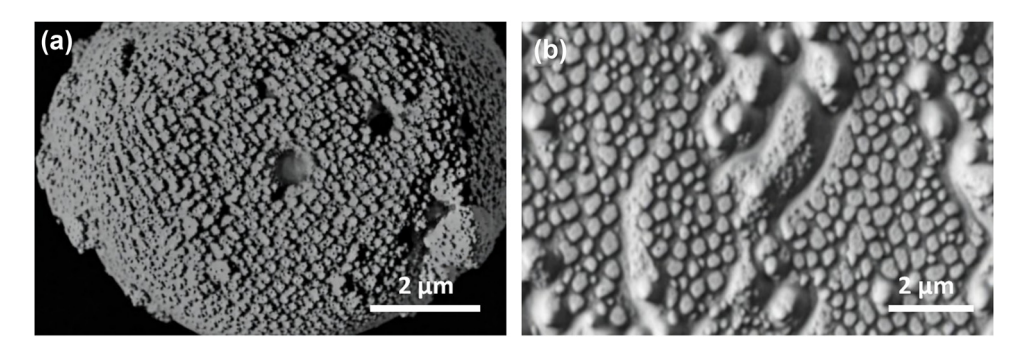


Figure 2: Backscattered SEM micrographs of (a) WC-10wt%Co-4wt%Cr agglomerates and (b) carbide dissolution at particle temperatures of 1,741°C.

shows a nearly linear rise with increasing kerosene flows, wherein higher fuel quantities boost the total gas volume. The maximum tested flow of 25.3 l·h⁻¹ yielded a velocity of 779 m·s⁻¹. Thus, balancing the oxygen and kerosene inputs is necessary to achieve suitably high velocities without compromising particle heating [20].

The distinctive two-phase microstructure of HVOFsprayed WC-CoCr cermet coatings comprises hard WC particles dispersed in a softer CoCr alloy matrix. The backscattered electron micrographs in Figures 2 and 3 highlight the carbide distribution and dissolution characteristics as a function of particle temperature during spraying. Figure 2a shows the SEM image of the 10 wt%Co-4wt%Cr powders. The size of WC-10wt%Co-4wt%Cr agglomerates is about 20 µm in diameter. Figure 2b shows negligible alteration of the angular carbide morphology for the coating sprayed at a lower temperature of 1,741°C. However, evidence of WC dissolution is clearly discernible in Figure 3 for the high temperature (1,842°C) condition, wherein the carbide particles develop rounded edges because of partial melting [21]. This phenomenon enriches the binder with W and C atoms dissolved from the decomposed carbide phase [22].

Despite microstructural differences, both coatings in Figures 2 and 3 manifest remarkably low porosity levels

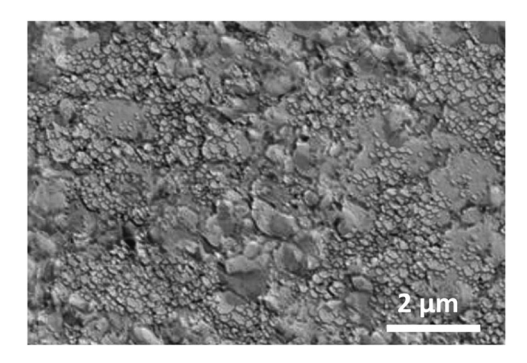


Figure 3: Backscattered SEM micrographs of carbide dissolution at particle temperatures of 1,842°C.

below 0.8%, which exceeds most porosity specifications for thermal spray coatings. This substantiates the capability of HVOF parameters to produce highly dense coatings. The rapid solidification and flattening of impinging particles aids pore elimination between successive coating layers [23]. Moreover, the high particle velocities minimize the loss of carbides during spraying by reducing dwell times in the torch flame [24]. This mitigates the formation of binder-rich regions with high shrinkage that ordinarily introduce coating porosity.

Figure 4 compiles the X-ray diffractograms obtained from the WC-CoCr powders and the as-sprayed coatings. The broad humps between 37° and 45° 2θ indicate an amorphous structure for the metallic CoCr binder resulting from its extremely high quenching rate during spraying [25]. Based on the carbide peaks, the index of retention compares dissolution across coatings, while the emerging W_2 C phase highlights the decomposition of WC at elevated

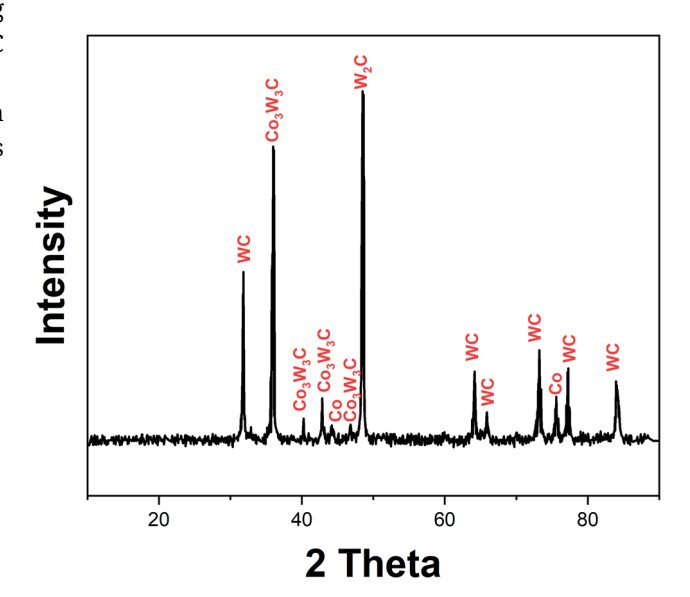


Figure 4: XRD patterns illustrating phases in feedstock powder and HVOF coatings.

DE GRUYTER HVOF — 5

Test	Particle temperature (°C)	Particle velocity (m·s ⁻¹)	Index of carbide retention	Porosity (%)	Hardness (HV0.3)
1	1,741 ± 11	722 ± 4	0.94 ± 0.01	0.60 ± 0.05	1,141 ± 79
2	1,792 ± 8	743 ± 3	0.93 ± 0.01	0.55 ± 0.04	1,157 ± 102
3	1,842 ± 10	799 ± 6	0.90 ± 0.02	0.35 ± 0.05	1,214 ± 65
4	1,904 ± 7	804 ± 5	0.90 ± 0.01	0.27 ± 0.05	1,195 ± 121

temperatures [26]. The data suggests that strategically limiting particle heating during spraying balances dense deposition and retention of the beneficial hard carbide phases.

The lamellar microstructure of HVOF coatings generates properties distinct from conventional bulk materials, wherein the splat boundaries and carbide distribution govern the mechanical performance. Table 1 documents the microhardness values alongside key microstructural metrics for the various WC-CoCr coatings produced in this study. The hardnesses correlate strongly with the index of carbide retention, as coatings sprayed under higher particle temperatures suffer from enhanced WC dissolution. This enriches the binder with W and C, increasing hardness through solid solution strengthening. Moreover, the presence of nano-crystalline W2C particles from WC decomposition also escalates hardness. However, simultaneously intensifying galvanic interactions and chemical dissolution negate the benefits of the minor hardness increment. An intermediate temperature of 1,835°C achieves near-complete carbide retention with adequate particle melting to yield a hardness exceeding 1200 HV0.3. The low porosity eliminates potential fatigue crack initiation sites that would undermine mechanical integrity. Overall, the data verifies that a compromise between particle heating and velocity is essential during HVOF spraying of cermet coatings to obtain optimal combinations of hardness, wear resistance, and electrochemical stability.

Potentiodynamic polarization tests are widely utilized for quantitatively evaluating electrochemical corrosion resistance. Figures 5 and 6 illustrate the measured polarization curves for the HVOF sprayed WC-CoCr coatings tested in aggressive 0.1 N HCl solution. The characteristic passive region spanning several hundred millivolts confirms the integrity of the protective oxide films, succeeded by transpassive dissolution at extreme anodic overpotentials [27]. Comparing the polarization curves in Figure 5 for coatings deposited under the same particle temperature (1,842°C) but different velocities of 799 and 743 m·s⁻¹, respectively, the faster velocity manifests lower i_{corr} and higher polarization resistance [28]. This highlights the role of particle deformation and adhesive stacking in mitigating galvanic effects associated with binder enrichment from carbide dissolution.

Figure 6 presents the polarization response for two coatings with identical particle velocities but different

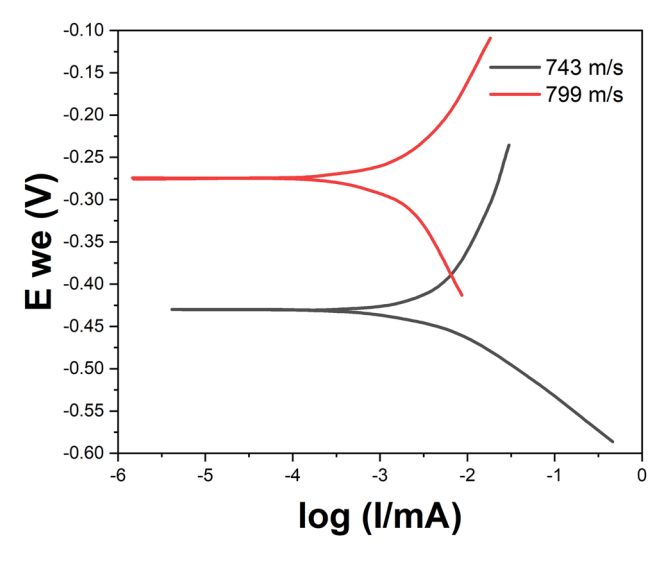


Figure 5: Potentiodynamic polarization curves showing the effect of particle velocity.

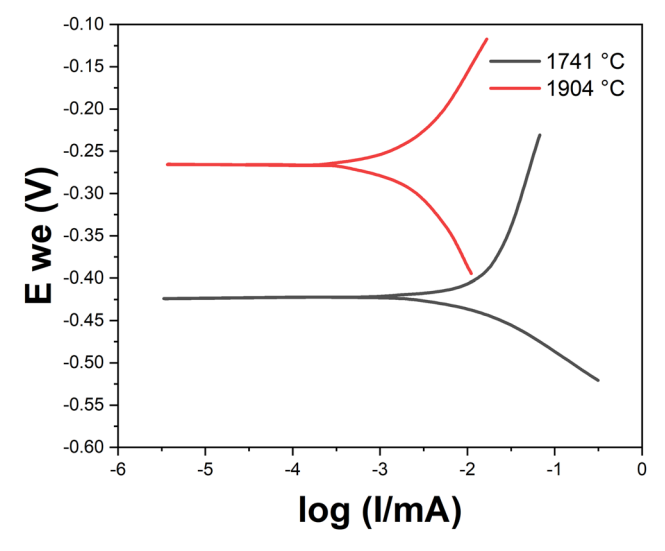


Figure 6: Potentiodynamic polarization curves showing the effect of particle temperature.

Table 2: Compilation of particle states during HVOF spraying and resultant corrosion parameters

Test	Particle temperature (°C)	Particle velocity (m·s ⁻¹)	i _{corr} (μΑ·cm ⁻²)	E _{corr} (mV)	Rp (Ω·cm²)
1	1,741	722	4.7	-455	1,699
2	1,792	743	3.8	-433	6,301
3	1,842	799	3.1	-272	15,224
4	1,904	804	3.2	-274	16,877

temperatures. The lower temperature condition again demonstrates superior behavior, substantiating that minimizing WC decarburization is vital for electrochemical stability in corrosive environments [29]. Table 2 compiles the quantitative electrochemical parameters along with the particle state during spraying. An intermediate temperature of 1,842°C balanced with a high velocity above 799 m·s⁻¹ optimizes the corrosion resistance. This validates conclusions from the microstructural characterization, emphasizing that suitable particle heating enables coating consolidation while extensive carbide dissolution degrades electrochemical properties [30]. The results verify that corrosion is initiated at the carbide-matrix interfaces or splat boundaries, wherein localized attack causes carbide debonding [31]. Strategies for improving corrosion performance include reducing porosity to below 0.5% while restricting carbide dissolution to over 90% retention. The data signifies that corrosion protection must be holistically co-optimized during spraying along with conventional metrics for wear protection like hardness.

The distinctive splat-based architecture makes HVOF coatings susceptible to localized corrosion phenomena compared to conventional monolithic materials [32]. Detailed analysis of potentiodynamically tested samples provides vital insights into the associated mechanisms. The secondary

electron images in Figures 7 and 8 reveal characteristic features of crevice corrosion along inter-splat zones. This arises from fluid ingression into pores or imperfect interfaces, creating localized electrochemical cells. The acidic environment so produced accelerates metal dissolution, eventually dislodging entire splats from the coating surface. Energy dispersive spectroscopy confirmed dealloying of the CoCr matrix occurring at these crevices.

The corrosion resistance of HVOF-sprayed cermet coatings is governed by a complex interplay of microstructural features, including the extent of carbide dissolution, porosity levels, and the formation of galvanic couples between the carbide and matrix phases. Our results demonstrate that these microstructural attributes are directly influenced by the in-flight particle temperature and velocity during the HVOF process. Higher particle temperatures, as shown in Figure 6, lead to increased dissolution of the WC particles in the CoCr matrix. This occurs due to the partial melting of the carbide phase, which results in the enrichment of the binder with tungsten and carbon

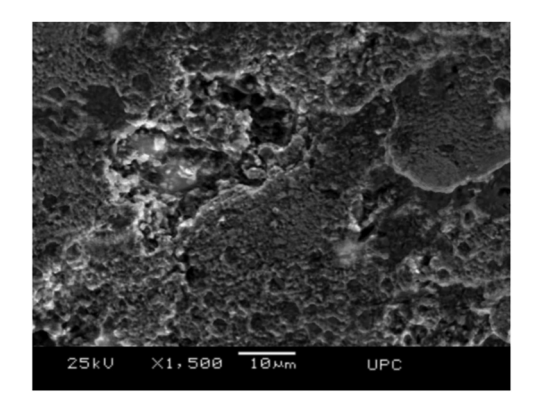


Figure 8: Pitting corrosion induced by carbide–matrix galvanic couples.

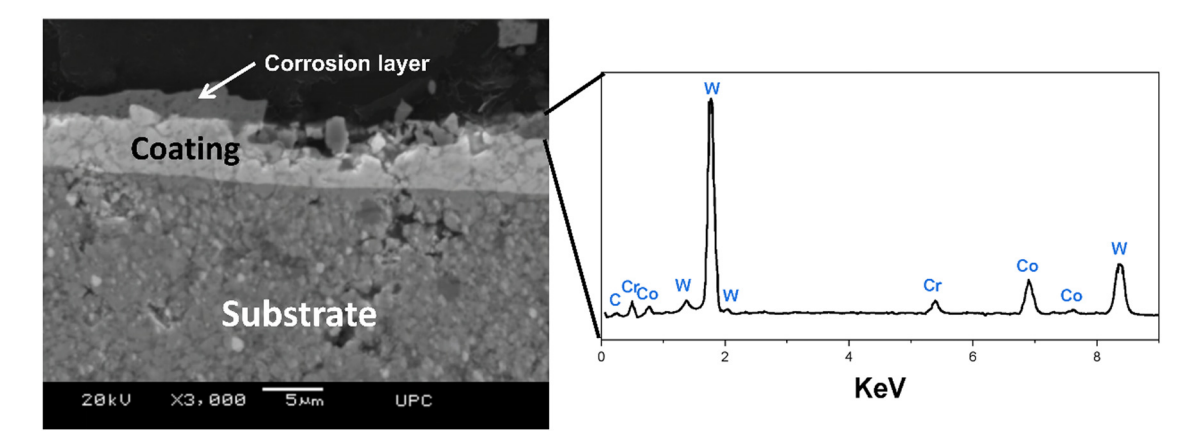


Figure 7: SEM image showing crevice corrosion along splat boundary.

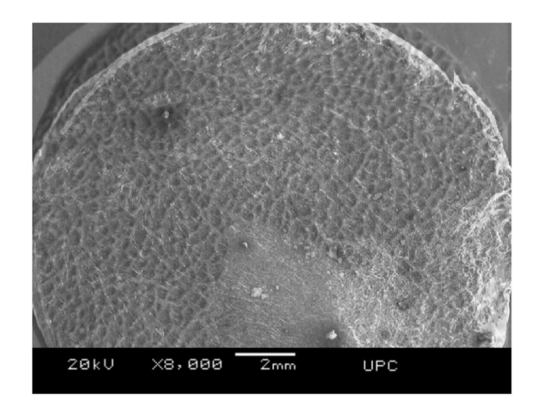


Figure 9: Surface oxide morphology and composition after polarization test.

atoms. The presence of these dissolved species alters the electrochemical behavior of the matrix, making it more susceptible to corrosion attack. Additionally, the formation of eta-phases due to carbide decomposition can create localized galvanic cells that accelerate corrosion. On the other hand, higher particle velocities promote the formation of denser and more cohesive coatings. The increased kinetic energy of the impacting particles results in improved intersplat bonding and reduces the overall porosity of the coating. This is evident from the data in Table 1, where coatings deposited at higher velocities exhibit lower porosity levels. Minimizing porosity is crucial for corrosion resistance, as it limits the ingress of corrosive media and prevents the formation of localized corrosion cells at splat boundaries. The optimal corrosion resistance is achieved by striking a balance between particle temperature and velocity. In our study, the best-performing coating was obtained at an intermediate temperature of 1,842°C and a

high velocity of 799 $\text{m} \cdot \text{s}^{-1}$. This combination allows for sufficient particle melting and deformation to produce a dense coating while minimizing the detrimental effects of excessive carbide dissolution.

Figure 8 also elucidates the pitting corrosion mechanism initiated by the debonding of WC particles. This triggers the formation of intense galvanic couples between the electrically conductive carbides and the oxidized metal matrix [33]. Unmitigated dissolution subsequent to pit nucleation leads to extensive subsurface attack and loss of coating integrity. Minimizing porosity levels to below 0.5% through HVOF parametric optimization suppresses such localized degradation phenomena [9]. Nonetheless, evidence from the current and previous studies proves that optimally limiting carbide dissolution is equally vital to mitigate coating damage from corrosion.

The protective oxide structure responsible for electrochemical stability is illustrated in the fractograph—micrograph in Figure 9. The entire coating surface is engulfed by an adherent chromium-enriched oxide film, confirmed by compositional analysis. This layer forms spontaneously upon exposure to aqueous environments and impedes charge transfer reactions [34]. However, breakdown of its passivity occurs at localized imperfections like pores or carbide—matrix interfaces. The nodular morphology visible in Figure 9 resembles reported structures of cobalt/tungsten oxide phases generated on WC-CoCr surfaces due to anodic polarization. Unfortunately, the acidic conditions diminish their protectiveness against sustained corrosion attacks. Yet, rational tuning of HVOF process parameters aids the growth of more resilient surface films.

EIS enables detailed analysis of coatings' corrosion mechanisms by appropriate modeling using equivalent

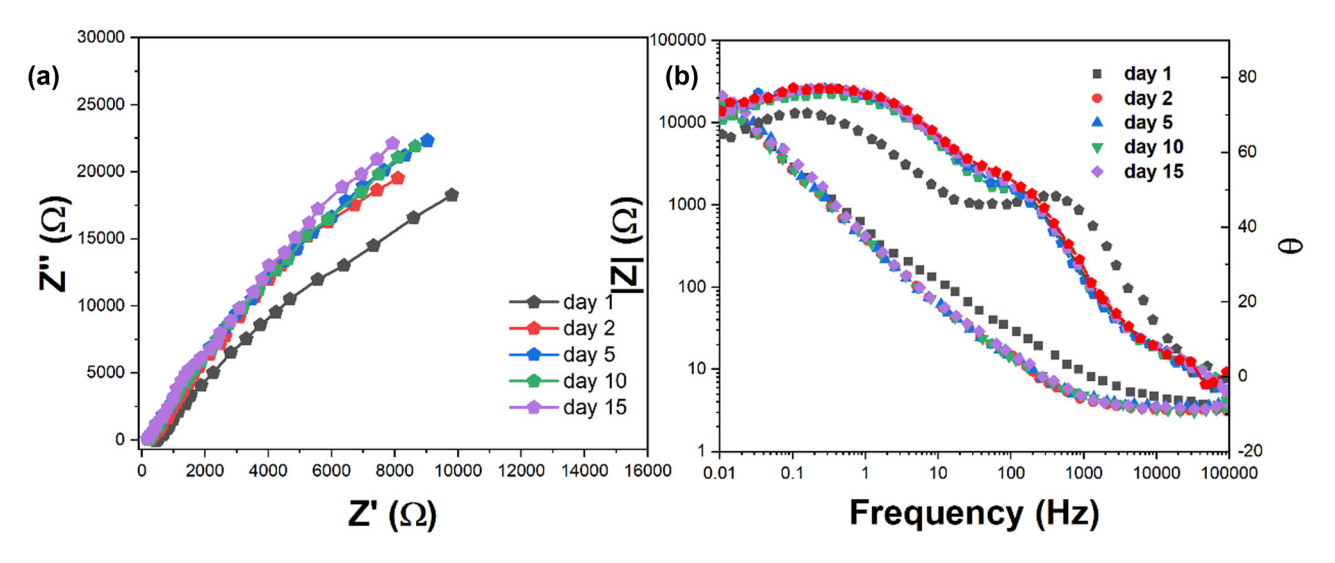


Figure 10: (a) Nyquist and (b) Bode phase plots showing EIS response with time.

8 — Zhihui Xing et al. DE GRUYTER

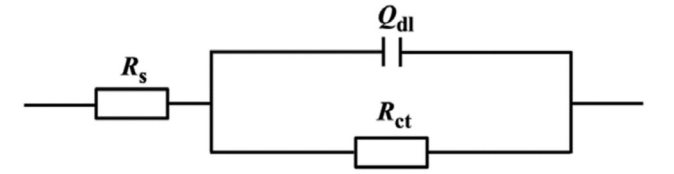


Figure 11: Equivalent circuits modeling corrosion mechanisms.

circuit representations. The Nyquist and Bode phase plots in Figure 10a and b, respectively, compile the EIS response of the optimized WC-CoCr coating upon prolonged exposure to SRB-inoculated actual seawater over 15 days. The sequential evolution of the spectra suggests active surface colonization by the SRBs, which alter charge transfer pathways [35]. Equivalent circuit models presented in Figure 11 decipher the physical significance behind the measured EIS response.

The excellent conformity between experimental data and the modeled plots validates the proposed equivalent circuits. The core elements in all cases are the polarization resistance (R_{ct}) and double layer capacitance (C_{dl}), which quantify the kinetics of electrochemical reactions occurring at the coating surface [36]. Their time-dependence presented in Figure 12 confirms that R_{ct} decreases during the initial period as the coating surface gets activated upon interaction with corrosive species and SRB metabolites. However, protective surface film formation by the corrosion products subsequently increases R_{ct} . The final reduction is attributable to localized film breakdown, which accelerates charge transfer [37]. Overall, the EIS results verify that the HVOF coatings offer adequate electrochemical stability even after prolonged bacterial exposure, suggesting suitability for maritime applications.

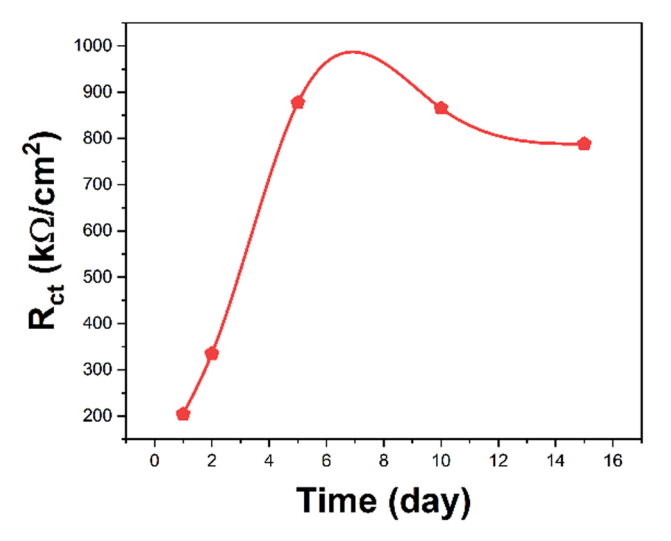


Figure 12: Extracted R_{ct} values demonstrating time dependence.

Sulfate-reducing bacteria pose a concern for offshore hydraulic components owing to accelerated corrosion resulting from their metabolic activity. The EIS results showcase noticeable variation upon inoculation with SRBs compared to as-prepared conditions. This confirms that the biofilms alter corrosion mechanisms involving charge transfer and mass transport processes [38]. Interestingly, trends in $R_{\rm ct}$ values noted earlier indicate self-healing behavior wherein corrosion products deposit on defects, thereby resisting further attack [39]. Such quantitative electrochemical interrogation of coating's performance in representative operating conditions is invaluable for science-guided coating customization and parameter optimization.

4 Conclusion

In conclusion, this comprehensive study provides vital insights into corrosion and biocorrosion phenomena affecting HVOF-sprayed WC-10Co-4Cr coatings, enabling science-based strategies to obtain optimal protection specifications sought in demanding offshore hydraulic applications. By balancing particle velocity and temperature through parametric control of the kerosene and oxygen flow rates, coatings with hardness exceeding 1,200 HV0.3 are attained alongside properties such as 0.35% porosity, over 90% carbide retention, and corrosion rates below 4 μA·cm⁻² in acidic media. Localized attack is mitigated by the lamellar cohesion from particles impacting at velocities upwards of 799 m·s⁻¹. Prolonged marine exposure introduces complex electrochemical interactions, with sulfate-reducing bacterial biofilms on coating surfaces causing the polarization resistance to decrease from 15.2 to 12.4 kΩ·cm⁻² over 15 days. Nonetheless, self-healing effects are noted as corrosion products deposit on defects, resisting sustained biocorrosion. The quantitative corrosion characterization techniques substantiate HVOF coatings as effective and eco-friendly replacements for toxic chromate platings currently used in offshore hydraulics. The research provides a framework enabling science-guided customization of thermally sprayed coatings for combined wear and corrosion specifications in corrosive applications spanning maritime, aerospace, and chemical sectors. This offers vital economic benefits and ecosystem preservation.

Funding information: The authors state no funding involved.

Author contributions: All authors have accepted responsibility for the entire content of this manuscript and approved its submission.

DE GRUYTER HVOF — 9

Conflict of interest: The authors state no conflict of interest.

Data availability statement: The data that support the findings of this study are available on request from the corresponding author.

References

- [1] Xu, L., L. Pi, Y. Dou, Y. Cui, X. Mao, A. Lin, et al. Electroplating of thick hard chromium coating from a trivalent chromium bath containing a ternary complexing agent: A methodological and mechanistic study. ACS Sustainable Chemistry & Engineering, Vol. 8, No. 41, 2020, pp. 15540–15549.
- [2] Wang, S., C. Ma, and F. Walsh. Alternative tribological coatings to electrodeposited hard chromium: a critical review. *Transactions of the IMF*, Vol. 98, No. 4, 2020, pp. 173–185.
- [3] Garcia Nieto, P. J., E. García Gonzalo, F. Sanchez Lasheras, and A. Bernardo Sánchez. A hybrid predictive approach for chromium layer thickness in the hard chromium plating process based on the differential evolution/gradient boosted regression tree methodology. *Mathematics*, Vol. 8, No. 6, 2020 Jun, id. 959.
- [4] Nguyen, V. P., T. N. Dang, C. C. Le, and D. A. Wang. Effect of coating thickness on fatigue behavior of AISI 1045 steel with HVOF thermal spray and hard chrome electroplating. *Journal of Thermal Spray Technology*, Vol. 29, No. 8, 2020, pp. 1968–1981.
- [5] Singh, J. and J. P. Singh. Performance analysis of erosion resistant Mo₂C reinforced WC-CoCr coating for pump impeller with Taguchi's method. *Industrial Lubrication and Tribology*, Vol. 74, No. 4, 2022, pp. 431–441.
- [6] Thakur, L. and N. Arora. An investigation on the development and wear performance of chromium-MWCNTs transformed HVOF sprayed nano-WC-CoCr coatings. Surface and Coatings Technology, Vol. 388, 2020 Apr, id. 125610.
- [7] Torkashvand, K., M. Gupta, S. Björklund, F. Marra, L. Baiamonte, and S. Joshi. Influence of nozzle configuration and particle size on characteristics and sliding wear behaviour of HVAF-sprayed WC-CoCr coatings. Surface and Coatings Technology, Vol. 423, 2021 Oct, id. 127585.
- [8] Russell, Z., M. Gaier, M. J. Froning, and K. P. Plucknett. The aqueous corrosion and wear responses of HVOF-deposited TiC-Ni₃Al, WC-Co, and WC-CoCr coatings on AISI 4130 steel substrates. Surface and Coatings Technology, Vol. 473, 2023 Nov, id. 130018.
- [9] Lekatou, A. G., D. Sioulas, and D. Grimanelis. Corrosion and wear of coatings fabricated by HVOF-spraying of nanostructured and conventional WC-10Co-4Cr powders on Al7075-T6. *International Journal* of Refractory Metals and Hard Materials, Vol. 112, 2023 Apr, id. 106164.
- [10] Kumar, V., R. Verma, and R. Kumar. Analysis of the corrosion and wear of WC-10Co-4Cr + GNPs coating applied to HSLA DH-36 steel using HVOF. *Surface Topography: Metrology and Properties*, Vol. 10, No. 4, 2022 Oct, id. 045007.
- [11] Zhao, L., H. Sun, S. Li, C. Si, and S. Xu. An investigation of the effect of post heat treatment on the wear and corrosion behavior of HVOF-sprayed WC-10Co4Cr coatings. *Journal of Thermal Spray Technology*, Vol. 32, No. 8, 2023 Dec, pp. 2394–2410.

[12] Kumar, M. and R. Upadhyaya. Corrosion and wear analysis of HVOLF sprayed WC-10CO-4Cr coating on geothermal turbine blade. World Journal of Engineering, Vol. 16, No. 6, 2019 Jan, pp. 768–774.

- [13] Cao, Q., L. Fan, H. Chen, Y. Xu, and L. Dong. Corrosion behavior of WC–Co coating by plasma transferred arc on EH40 steel in lowtemperature. *High Temperature Materials and Processes*, Vol. 41, No. 1, 2022 Jan, pp. 191–205.
- [14] Moghaddasi, M., M. Bozorg, E. Aghaie, H. Bakhtiyari, and H. Torbati-Sarraf. Corrosion and wear analysis of high-velocity oxyfuel sprayed WC-10Co-4Cr and colmonoy-6 coatings on nickel-aluminum bronze alloy substrate. *Journal of Materials Engineering and Performance*, Vol. 30, No. 10, 2021 Oct, pp. 7564–7576.
- [15] Zhou, Y. K., X. B. Liu, J. J. Kang, W. Yue, W. B. Qin, G. Z. Ma, et al. Corrosion behavior of HVOF sprayed WC-10Co4Cr coatings in the simulated seawater drilling fluid under the high pressure. *Engineering Failure Analysis*, Vol. 109, 2020 Jan, id. 104338.
- [16] Tian, Y., H. Zhang, X. Chen, A. McDonald, S. Wu, T. Xiao, et al. Effect of cavitation on corrosion behavior of HVOF-sprayed WC-10Co4Cr coating with post-sealing in artificial seawater. *Surface and Coatings Technology*, Vol. 397, 2020 Sep, id. 126012.
- [17] Zhao, X., C. Li, H. Jiang, S. Li, and X. Han. Mechanistic study on the influence of hydrogen fuel in high-velocity oxygen-fuel (HVOF) thermal spraying process. *JOM*, Vol. 76, No. 1, 2024 Jan, pp. 57–70.
- [18] Legros, S., C. Brunet, P. Domingo-Alvarez, P. Malbois, E. Salaun, G. Godard, et al. Combustion for aircraft propulsion: Progress in advanced laser-based diagnostics on high-pressure kerosene/air flames produced with low-NOx fuel injection systems. *Combustion and Flame*, Vol. 224, 2021 Feb, pp. 273–294.
- [19] Zhao, X., C. Li, S. Li, X. Han, and P. Liu. Mechanism evaluations of conventional and suspended HVOF thermal spraying based on EDC and EDM combustion models. *Applied Thermal Engineering*, Vol. 241, 2024 Mar, id. 122405.
- [20] Kannan, S., T. Ba, S. Wan, C. W. Kang, J. Pan, and Z. Zhang. Numerical and experimental investigations of CoNiCrAlY particle suspension dynamics in kerosene-oxygen high velocity oxygen fuel spraying. *Coatings*, Vol. 13, No. 4, 2023 Apr, id. 668.
- [21] Yang, G., W. Song, N. Wang, Y. Li, and Y. Ma. Fabrication and formation mechanism of vacuum cladding Ni/WC/GO composite fusion coatings. *Materials Today Communications*, Vol. 25, 2020 Dec, id. 101342.
- [22] Qian, C., Y. Liu, H. Cheng, K. Li, and B. Liu. Effect of the carbon content on the morphology evolution of the η phase in cemented carbides with the CoNiFeCr high entropy alloy binder. *International Journal of Refractory Metals and Hard Materials*, Vol. 102, 2022 Jan, id. 105731.
- [23] Mittal, G. and S. Paul. Suspension and solution precursor plasma and HVOF spray: A review. *Journal of Thermal Spray Technology*, Vol. 31, No. 5, 2022 Jun, pp. 1443–1475.
- [24] Baumann, I., L. Hagen, W. Tillmann, P. Hollingsworth, D. Stangier, G. Schmidtmann, et al. Process characteristics, particle behavior and coating properties during HVOF spraying of conventional, fine and nanostructured WC-12Co powders. *Surface and Coatings Technology*, Vol. 405, 2021 Jan, id. 126716.
- [25] Berget, J., T. Rogne, and E. Bardal. Erosion–corrosion properties of different WC–Co–Cr coatings deposited by the HVOF process influence of metallic matrix composition and spray powder size distribution. Surface and Coatings Technology, Vol. 201, No. 18, 2007 Jun, pp. 7619–7625.
- [26] Maiti, A. K., N. Mukhopadhyay, and R. Raman. Improving the wear behavior of WC-CoCr-based HVOF coating by surface grinding.

- *Journal of Materials Engineering and Performance*, Vol. 18, No. 8, 2009 Nov, pp. 1060–1066.
- [27] Yang, X., X. Dong, W. Li, W. Feng, and Y. Xu. Effect of solution and aging treatments on corrosion performance of laser solid formed Ti-6Al-4V alloy in a 3.5 wt. % NaCl solution. *Journal of Materials* Research and Technology, Vol. 9, No. 2, 2020 Mar, pp. 1559–1568.
- [28] Meghwal, A., A. Anupam, C. Schulz, C. Hall, B. S. Murty, R. S. Kottada, et al. Tribological and corrosion performance of an atmospheric plasma sprayed AlCoCr0.5Ni high-entropy alloy coating. *Wear*, Vol. 506–507, 2022 Oct, id. 204443.
- [29] Wang, D., Q. Zhao, T. Yang, X. Chang, S. Qu, S. Sun, et al. Influences of thermomechanical conditions on corrosion behavior of lowcarbon steels in artificial seawater. *International Journal of Electrochemical Science*, Vol. 14, No. 3, 2019 Mar. pp. 2509–2525.
- [30] Heakal, F. E. T. and A. M. Bakry. Corrosion degradation of AXJ530 magnesium alloy in simulated pysiological fluid and its mitigation by fluoride and chitosan coatings for osteosynthetic applications. *International Journal of Electrochemical Science*, Vol. 13, No. 8, 2018 Aug, pp. 7724–7747.
- [31] Luo, T., P. Xu, and C. Guo. Controllable construction and corrosion resistance mechanism of durable superhydrophobic micro-nano structure on aluminum alloy surface. *Sustainability*, Vol. 15, No. 13, 2023 Jan, id. 10550.
- [32] Abbas, M., G. M. Smith, and P. R. Munroe. Microstructural characterization of HVOF-sprayed ni on polished and oxidized stainless steel substrates. *Journal of Thermal Spray Technology*, Vol. 29, No. 5, 2020 Jun, pp. 1093–1110.

- [33] Katiyar, P. K.. A comprehensive review on synergy effect between corrosion and wear of cemented tungsten carbide tool bits: A mechanistic approach. *International Journal of Refractory Metals and Hard Materials*, Vol. 92, 2020 Nov, id. 105315.
- [34] Kihn, Y., G. E. Thompson, G. Galaup, P. Skeldon, X. Zhou, K. Shimizu, et al. Morphology, composition and structure of anodic films on Al–Cr alloys. *Corrosion Science*, Vol. 42, No. 3, 2000 Mar, pp. 533–544.
- [35] Sun, C., J. Xu, F. H. Wang, and C. K. Yu. Effect of sulfate reducing bacteria on corrosion of stainless steel 1Cr18Ni9Ti in soils containing chloride ions. *Materials Chemistry and Physics*, Vol. 126, No. 1, 2011 Mar, pp. 330–336.
- [36] Xu, J., K. Wang, C. Sun, F. Wang, X. Li, J. Yang, et al. The effects of sulfate reducing bacteria on corrosion of carbon steel Q235 under simulated disbonded coating by using electrochemical impedance spectroscopy. *Corrosion Science*, Vol. 53, No. 4, 2011 Apr, pp. 1554–1562.
- [37] AlAbbas, F. M., C. Williamson, S. M. Bhola, J. R. Spear, D. L. Olson, B. Mishra, et al. Influence of sulfate reducing bacterial biofilm on corrosion behavior of low-alloy, high-strength steel (API-5L X80). *International Biodeterioration & Biodegradation*, Vol. 78, 2013 Mar, pp. 34–42.
- [38] Tran, T. T. T., K. Kannoorpatti, A. Padovan, and S. Thennadil. Effect of pH regulation by sulfate-reducing bacteria on corrosion behaviour of duplex stainless steel 2205 in acidic artificial seawater. *Royal Society Open Science*, Vol. 8, No. 1, 2021 Jan, id. 200639.
- [39] Chen, L., B. Wei, and X. Xu. Effect of sulfate-reducing bacteria (SRB) on the corrosion of buried pipe steel in acidic soil solution. Coatings, Vol. 11, No. 6, 2021 Jun, id. 625.